Received: 25 October 2019 | Revised: 16 March 2020 | Accepted: 2 April 2020

DOI: 10.1002/mrm.28298

FULL PAPER

Magnetic Resonance in Medicine

Whole brain snapshot CEST at 3T using 3D-EPI: Aiming for speed, volume, and homogeneity

Sebastian Mueller[1] | **Rüdiger Stirnberg**[2] | **Suzan Akbey**[2] | **Philipp Ehses**[2] | **Klaus Scheffler**[1,3] | **Tony Stöcker**[2,4] | **Moritz Zaiss**[1,5]

[1]High-field Magnetic Resonance Center, Max Planck Institute for Biological Cybernetics, Tuebingen, Germany

[2]German Center for Neurodegenerative Diseases (DZNE), Bonn, Germany

[3]Department of Biomedical Magnetic Resonance, Eberhard Karls University Tuebingen, Tuebingen, Germany

[4]Department of Physics and Astronomy, University of Bonn, Bonn, Germany

[5]Department of Neuroradiology, University Hospital Erlangen, Erlangen, Germany

Correspondence
Sebastian Mueller, Max Planck Institute for Biological Cybernetics, High-field Magnetic Resonance Center, Max-Planck-Ring 11, 72076 Tuebingen, Germany.
Email: sebastian.mueller@tuebingen.mpg.de

Funding information
This work received support from the Max Planck Society, German Research Foundation (DFG), grant ZA 814/2-1; and European Union's Horizon 2020 research and innovation program, grant agreement No. 667510

Purpose: CEST MRI enables imaging of distributions of low-concentrated metabolites as well as proteins and peptides and their alterations in diseases. CEST examinations often suffer from low spatial resolution, long acquisition times, and concomitant motion artifacts. This work aims to maximize both resolution and volume coverage with a 3D-EPI snapshot CEST approach at 3T, allowing for fast and robust whole-brain CEST MRI.

Methods: Resolution and temporal SNR of 3D-EPI examinations with nonselective excitation were optimized at a clinical 3T MR scanner in five healthy subjects using a clinical head/neck coil. A CEST presaturation module for low power relayed nuclear Overhauser enhancement and amide proton transfer contrast was applied as an example. The suggested postprocessing included motion correction, dynamic B_0 correction, denoising, and B_1 correction and was compared to an established 3D-gradient echo-based sequence.

Results: CEST examinations were performed at 1.8 mm nominal isotropic resolution in 4.3 s per presaturation offset. In contrast to slab-selective 3D or multislice approaches, the whole brain was covered. Repeated examinations at three different B_1 values took 13 minutes for 58 presaturation offsets with temporal SNR around 75. The resulting CEST effects revealed significant gray and white matter contrast and were of similar quality across the whole brain. Coefficient of variation across three healthy subjects was below 9%.

Conclusion: The suggested protocol enables whole brain coverage at 1.8 mm isotropic resolution and fast acquisition of 4.3 s per presaturation offset. For the fitted CEST amplitudes, high reproducibility was proven, increasing the opportunities of quantitative CEST investigations at 3T significantly.

KEYWORDS

3D CEST MRI, chemical exchange saturation transfer MRI 3T, chemical exchange saturation transfer MRI EPI, high resolution CEST MRI, whole-brain CEST MRI

1 | INTRODUCTION

CEST MRI allows indirect detection of low concentrated solutes. CEST uses two properties of these low concentrated solutes: their chemical exchange with the bulk water proton pool, and their chemical shift relative to water by a certain frequency offset δω. In contrast to purely anatomical MRI, a frequency selective presaturation module with RF irradiation at δω precedes each image readout. Given presaturation at different frequencies, the resulting bulk water signals may be combined to a Z-spectrum,[1] which contains information on all interacting metabolites resonating in the covered frequency range. To extract all information, the Z-spectrum should be sampled densely, and the presaturation and readout block are thus repeated 10 to 100 times. The major problem of the combination of CEST presaturation and classic line-by-line MRI readout is that the repeated excitations will successively destroy the prepared magnetization state. The number of excitations can be reduced by k-space segmentation or by a small matrix size (small FOV or low resolution). Recently, a snapshot CEST approach with centric reordered 3D-gradient echo (GRE) readout scheme was proposed that was optimized for maximized number of k-space lines being acquired following a single presaturation.[2] Still, this GRE-based method was limited to 16 slices and a resolution of $1.7 \times 1.7 \times 5$ mm^3. When extending the volume coverage to whole brain, even at 3T CEST effects become sensitive to the inhomogeneity of B_1 RF irradiation. To correct for spatial inhomogeneity in B_1, repeated measurements at different nominal B_1 values are needed.[3] In this work, encouraged by recent findings at 7T,[4] we extended a 3D-EPI readout to allow semielliptical scanning along with CAIPIRINHA[5] undersampling. It was then optimized with centric reordering and nonselective excitation for whole-brain snapshot CEST MRI at 3T. This increased temporal SNR (tSNR) by 20% compared to the 7T protocol applied at 3T. In addition, a novel saturation scheme at low power B_1 was applied to minimize side bands in the Z-spectrum. Together with the proposed postprocessing, this enables multipool CEST MRI with whole brain coverage and isotropic resolution of 1.8 mm in less than 4:30 minutes for a fully sampled Z-spectrum at a clinical MR system.

2 | METHODS

2.1 | MR examinations

All examinations were performed at a clinical whole-body MR system (3T Magnetom Prisma^{fit}, Siemens Healthineers, Germany). The vendor-provided 1Tx/64Rx-channel head/neck coil was used for MR image acquisition on six healthy subjects with written informed consent and approval by the local ethics committee.

The CEST presaturation module was optimized for relayed nuclear Overhauser enhancement (rNOE) and amide proton transfer (APT) contrast by modifying a scheme suggested by Deshmane et al.[6] To reduce sidebands and increase selectivity, rather long Gaussian pulses of 16×100 ms were applied in the present study at a duty cycle of 50% and $B_1 = 0.65$ μT. The offset distribution can be found in the Supporting Information. To correct for B_1 inhomogeneity, data were acquired at [0.75, 1.00, 1.25] times the nominal B_1 by adjusting the reference voltage. This covered 95% of all measured relative B_1 values in vivo using the body coil as transmit coil. For imaging, both a 3D-GRE[2] and the 3D-EPI[7] sequence were investigated with nonselective excitation applied in both cases.

2.2 | MR readout parameters

The 3D-EPI readout was accelerated using parallel acquisition with CAIPIRINHA acceleration 1×6 (shift = 2, 36×36 reference lines) along both phase-encoding directions (PE, 3D) and 6/8 partial Fourier along the first PE direction. Semielliptical k-space sampling,[7] along with centric reordering of the 3D phase-encoding steps, were used. A non-blipped CAIPIRINHA sampling strategy for high spatiotemporal resolution[8] was chosen for which each CAIPIRINHA offset was realized with a separate excitation instead of 3D gradient blips. This resulted in a maximum EPI-factor of 32 and 45 excitations for the readout of 1201 k-space lines per 3D volume at a nominal matrix size of $144 \times 126 \times 88$ (RO × PE × 3D: head–foot × anteroposterior × left–right). A readout bandwidth of 1930 Hz/pixel with TE/echo train length = 11.0/24.3 ms lead to a total readout duration of 1.2 s for an isotropic nominal resolution of 1.8 mm at a FOV of $256 \times 224 \times 156$ mm^3. The nominal excitation flip angle (FA) was set to 15 degrees. Nonselective binomial-11 water excitation was applied instead of fat saturation to minimize chemical shift artifacts and maximize readout efficiency.[9] The acquisition duration was 4.3 s per presaturation offset, plus an additional 12 s recovery time for the unsaturated M_0 image. Fifty-seven offsets and one M_0 image could be measured in 4:22 min, including the CAIPIRINHA reference lines.

The 3D-GRE readout was accelerated using GRAPPA[10] 3×2 in both phase-encoding directions. Further undersampling was achieved by applying partial Fourier (6/8 along both phase-encoding directions) and omitting the corners of k-space (elliptical sampling). The number of acquired k-space lines for a nominal matrix size of $96 \times 78 \times 72$ (RO × PE × 3D: head–foot × anteroposterior × left–right) was therefore 487, and thus only 15% above the maximum of 424 lines derived according to the work of Zaiss et al[2] ($T_{1,WM} = 950$ ms[11]; FA = 5°; TR = 3.1 ms). The whole readout duration was 1.7 s. These optimized settings of the 3D-GRE (TE = 1.3 ms; TR = 3.1 ms; bandwidth = 660 Hz/pixel; FA = 5°)[12]

allowed to acquire one presaturation offset in 5.1 s (additional relaxation in case of M_0 image) with a nominal spatial resolution of 2.34 mm isotropic.

Field mapping was performed applying the simultaneous water shift and B_1 mapping (WASABI) approach of Schuenke et al[13] (t_p = 5000 μs, B_1 = 3.7 μT, recovery time (saturated/M_0): 3 s/12 s, 31 equally spaced presaturation offsets from −1.8 to +1.8 ppm). This was executed with the same imaging parameters as the CEST MRI sequences. To enable correction for spatiotemporal changes in B_0,[14] interleaved WASABI acquisitions were performed before and after each CEST examination.

For quantification of tSNR, 16 repeated measurements were performed without any presaturation module and a pause of 3 seconds in between consecutive image acquisitions. Different voxel sizes, acceleration factors, and nominal excitation FAs with otherwise identical parameters, unless stated differently, were investigated in preparation of the final 3D-EPI CEST protocol.

2.3 | CEST data evaluation

Data processing was performed using in-house written MatLab R2018a (The MathWorks, Inc., Natick, MA, USA) code, if not stated differently.

For both imaging methods, 3D-EPI and 3D-GRE, the postprocessing was identical. All images of the same examination were registered to the unsaturated image of the first WASABI to correct for subject movement during the acquisition. This was done automatically using the AFNI toolbox of Cox et al.[15] Afterward, the brain data were segmented automatically using SPM12[16] in case of the EPI and manually in case of the GRE readout to extract only the brain volume (including CSF, gray [GM], and white matter [WM]). The segmentation was of importance for the subsequently performed principal component analysis (PCA) based denoising. The CEST data sets were then corrected for dynamic changes in B_0[14] using $\Delta B_0(r,t)$ maps derived from the interleaved WASABI measurements. To reduce noise in the images, PCA denoising[17] was applied next. Median criterion with correction factor $\beta = 1.29$[18] was used to determine the cutoff eigenvalue in the reconstruction. Malinowski indicator function was exemplarily applied to one data set as well. With the so-called real error RE,[19] the cutoff eigenvalue k_{ind} can be derived as the minimum of $RE(k)/(c-k)^2$, where c is the number of columns (rows are observations in Casorati notation; columns are reshaped 3D volumes at a single offset frequency) in the considered matrix.[20] The denoised data were then corrected for spatial B_1 inhomogeneity, including three different nominal B_1 values for Z-B_1 correction.[3]

To quantify the CEST effects, a 4-pool Lorentzian model[21] was fitted to the postprocessed data voxel by voxel using a nonlinear least squares algorithm. The peak positions of APT, rNOE, and semisolid magentization transfer (ssMT) were fixed with respect to the frequency offset of direct water saturation (Supporting Information Table S1). To evaluate CEST effects within a certain tissue type, the tissue probability maps as derived with SPM12 were cut at a certain threshold (50% for GM and WM; 25% in case of CSF). Lower threshold for CSF was chosen to ensure contributions by CSF were separated from GM and WM.

For estimations on the point spread functions (PSF) of different readouts, numeric simulations had been performed for which a description can be found in the Supporting Information. These simulations were also used to investigate the effect of different FAs.

To evaluate the reproducibility of the derived results the Lorentzian amplitudes of APT, rNOE and ssMT pools were compared for different acquisitions. Within the tissue masks of GM and WM, the median amplitudes were determined. These were in the next step compared to the results of the other acquisitions in terms of mean value and SD, combined as a coefficient of variation (COV), which is the ratio of SD over mean value.

3 | RESULTS

3.1 | tSNR evaluation

tSNR was determined in each voxel as the ratio of mean value over SD for repeated measurements. As shown in Figure 1A, the tSNR decreased on average by approximately 30% going from $(2.0\ mm)^3$ to $(1.8\ mm)^3$ isotropic resolution. The increased average tSNR for higher FAs went along with a less homogeneous spatial distribution (Figure 1B,C and Supporting Information Figure S1). For FA > 20° a significant decrease of tSNR in the center and in lower regions of the brain was observed. For the final protocol, a FA of 15° was chosen. The PSF simulations (Figure 2) revealed a relative FWHM[2] of on average 1.33 for FA = 15°. The maximum relative magnitude was found to be 4.4% for FA = 17.5° (Supporting information Figure S4A). These numbers also prove a FA of 15° to be suitable. Increasing the total acceleration factor from 4 to 6 decreased tSNR by around 17% (Supporting Information Figure S2), which approximately corresponds to the expected thermal noise increase, that is, the expected additional g-factor penalty seems to be compensated for by reduced physiological noise (ratio of square root of undersampling factors: 18%). The non-blipped sixfold CAIPIRINHA acceleration nearly preserved signal with similar echo train length (24.3 vs. 23.9 ms, same EPI factor of 32) and allowed fewer excitations for the complete readout (45 vs. 66). The latter likely reduced physiological contributions to the tSNR.[22] For the final protocol (FA = 15°, non-blipped CAIPIRINHA = $1 \times 6^{(shift = 2)}$, partial Fourier = 6/8, 1.8 mm isotropic resolution), the tSNR of the EPI readout was ≈ 75 even in the cerebellum. In contrast to the previously published protocol for 7T[4], we worked out and optimized a modified 3D-EPI readout, for example,

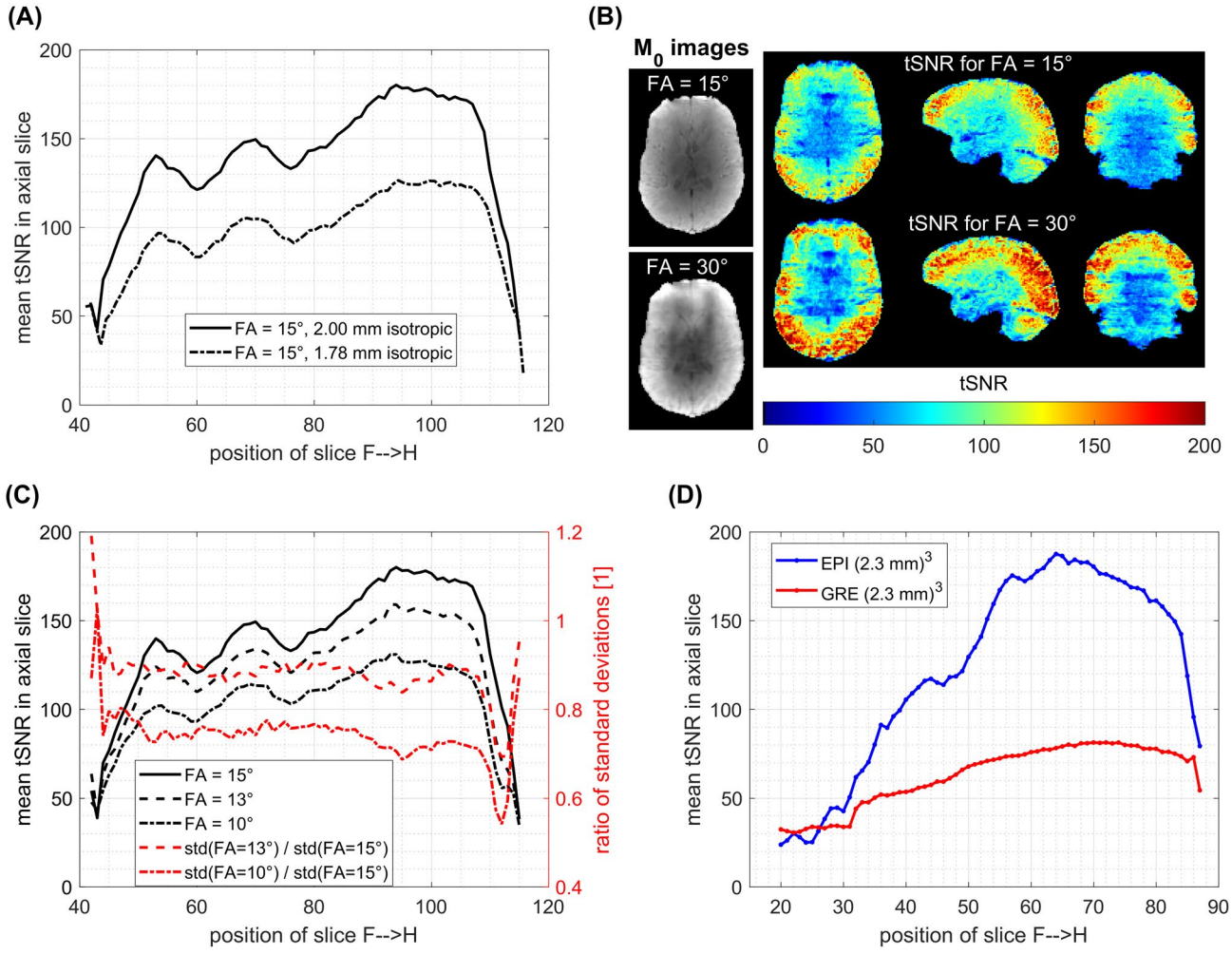

FIGURE 1 (A) tSNR of EPI for different spatial resolutions. (B) tSNR maps of EPI for different FAs at $(1.8\ \text{mm})^3$ nominal isotropic resolution. Higher FAs provide higher average tSNR but at the cost of increased spatial heterogeneity (see also (C)), with very low tSNR in the center and lower regions of the brain. Additionally, a single image of the time series is shown for both FAs. (C) Closer look at FAs around 15 degrees with mean and SD in different axial slices. (D) Comparison to the GRE readout at 2.34 mm. EPI at 1.8 mm isotropic resolution outperforms the 2.34 mm GRE in terms of tSNR. In the cerebellum, the tSNR is around 80. FA, flip angle; GRE, gradient echo; tSNR, temporal SNR

in terms of undersampling (GRAPPA vs. CAIPIRINHA), full versus elliptical sampling, and segmentation of one versus three. This yielded ≈20% higher tSNR for the novel 3T protocol (Supporting Information Figure S3). The PSF analysis revealed that the referring FWHM increased by 8.7% in the first and 9.5% in the second phase-encoding direction (compared to the 7T protocol) with maximum 1.75 pixels in the first PE direction (Figure 2E,F). Compared to the unfiltered PSF, the two protocols yielded a relative FWHM of 132 and 143%, respectively, in the first phase-encoding direction and 112 and 123% in the second.

3.2 | Inhomogeneity of B_1^+

As shown in Figure 3A to C, the B_1 amplitude varied by approximately 50% across the whole brain volume. The deviation along the head–foot direction was larger than the deviation along the other two (left–right and anteroposterior) directions (Figure 3A).

If the data were not corrected for B_1 inhomogeneity, fitted CEST contrasts were significantly altered as shown for rNOE in Figure 3D,E. For comparison of B_1 correction methods, the FWHM of Z-value distribution in GM and WM was determined by fitting a Gaussian distribution at each presaturation offset. In Supporting Information Figure S5A, it is shown that using as little as n = 2 B_1 values for correction already yielded 40/48% narrower FWHM in Z-value distributions in GM and WM than without B_1 correction. The FWHM decreased by 44.0/49.8% when including n = 3 B_1 values, but only by an additional 0.4/1.0 and 1.3/2.4% for n = 4 and n = 5 included B_1 values (spline interpolation; average over all offsets in GM/WM segments. Data not shown.). However, a 2-point correction

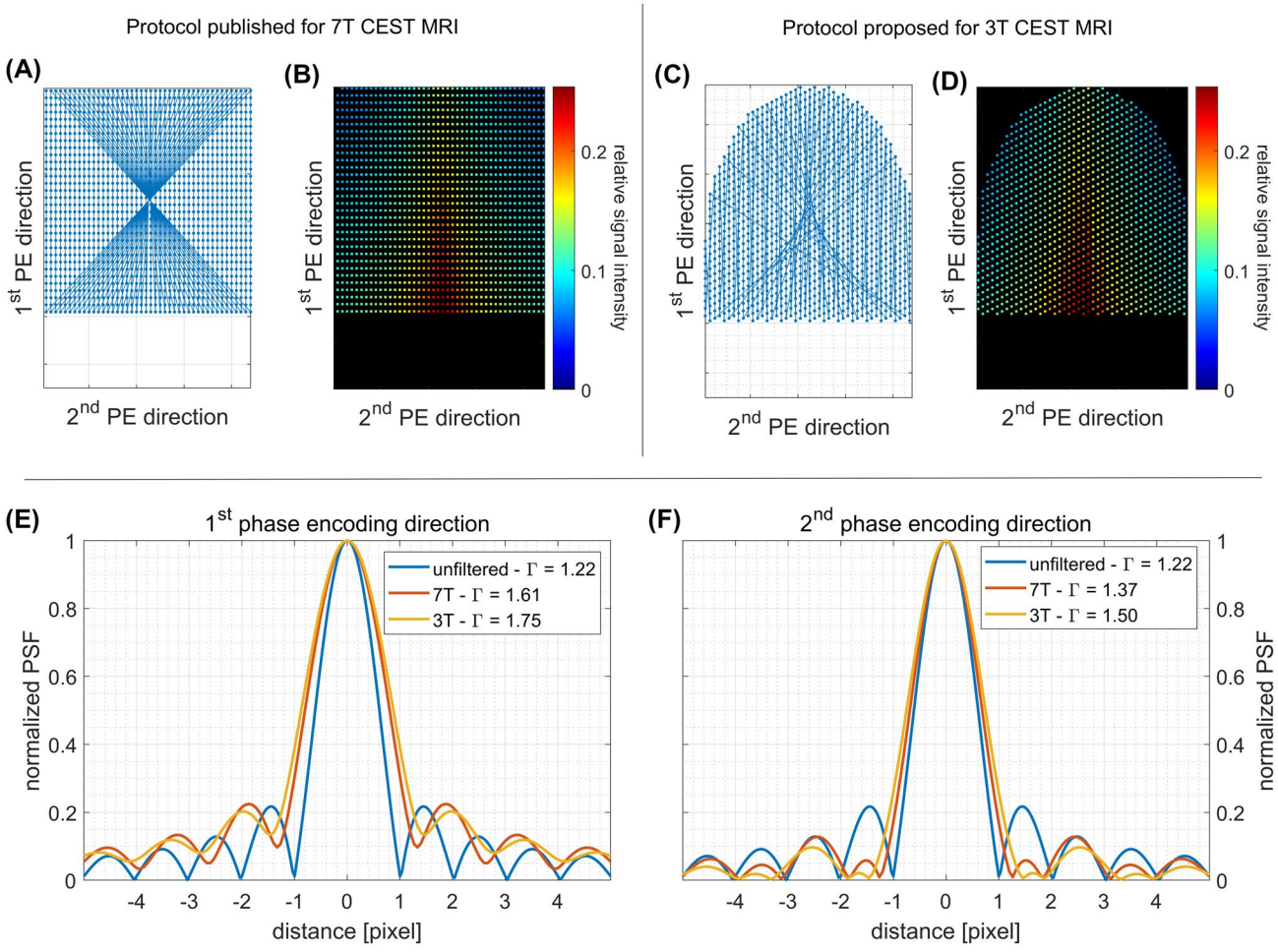

FIGURE 2 Comparing the PSFs of the established 7T protocol (A,B) and the novel 3T readout (C,D). (A,C) show the sampling trajectories, with CAIPIRINHA sampling in (C); and in (B,D) the resulting relative signal intensity is shown. PSFs (E,F) were determined from Fourier transformation of a 2D delta function that was convoluted with the signal evolution (B,D) determined from k space sampling taking into account both T_1 and T_2 (nominal matrix size (RO × PE × 3D): 144 × 126 × 88, FA = 15°, T_1 = 1300 ms, T_2^* = 45 ms and initial magnetization M_0 = 1 for both protocols. Variable TR for different excitations in 3T protocol with semielliptical sampling). Gamma is the FWHM of the PSF in both subplots. For the 3T protocol, like regular centric-out sampling, each 3D phase encoding slice starts with a new excitation; however, the first phase encoding is offset by ±1 line according to the CAIPIRINHA pattern. CAIPIRINHA, controlled aliasing in parallel imaging results in higher acceleration; PE, phase-encoding directions; PSF, point spread function; RO, readout; T, tesla

assumes linear behavior of Z-spectra over a 50% change in B_1. If only n = 2 B_1 values were included, the fitted amplitudes were altered (Supporting Information Figure S5B). Supporting information Figure S5B to E also show that including an increasing number of B_1 values in the correction reduced noise in the fitted contrast maps. This held true for spline but not necessarily for linear interpolation. We therefore suggest to measure at three different B_1 amplitudes and to use spline interpolated Z-B_1 correction.

3.3 | CEST contrast

With the Z-B_1 corrected whole brain 3D-EPI approach, CEST contrast maps (fitted amplitudes) with high homogeneity over the whole FOV were generated. As shown in Figure 4, the contrast maps covered the whole brain volume with high spatial resolution. Fine anatomical structures, such as GM and WM regions in the cerebellum, could be distinguished in all fitted contrasts (APT, ssMT, and rNOE). In agreement with previous studies,[6,23,24] higher rNOE (×1.17) and ssMT (x1.61) amplitudes in WM compared to GM were found (Table 1), as well as the inverse relationship (x0.88) for APT (see also Figure 5). On average (n = 3 healthy subjects examined with final protocol) the median fitted Lorentzian amplitudes in GM and WM were (mean ± SD): {(5.9 ± 0.1)%/(5.21 ± 0.02)%} for APT, {(9.2 ± 0.3)%/(10.8 ± 0.1)%} for rNOE, and {(5.21 ± 0.09)%/(8.4 ± 0.1)%} for ssMT.

As shown in Figure 6, fitted CEST pool amplitudes revealed reproducible GM/WM contrast for different healthy subjects. Reproducibility was investigated both across the same subject at different sessions and for direct repetition within the same

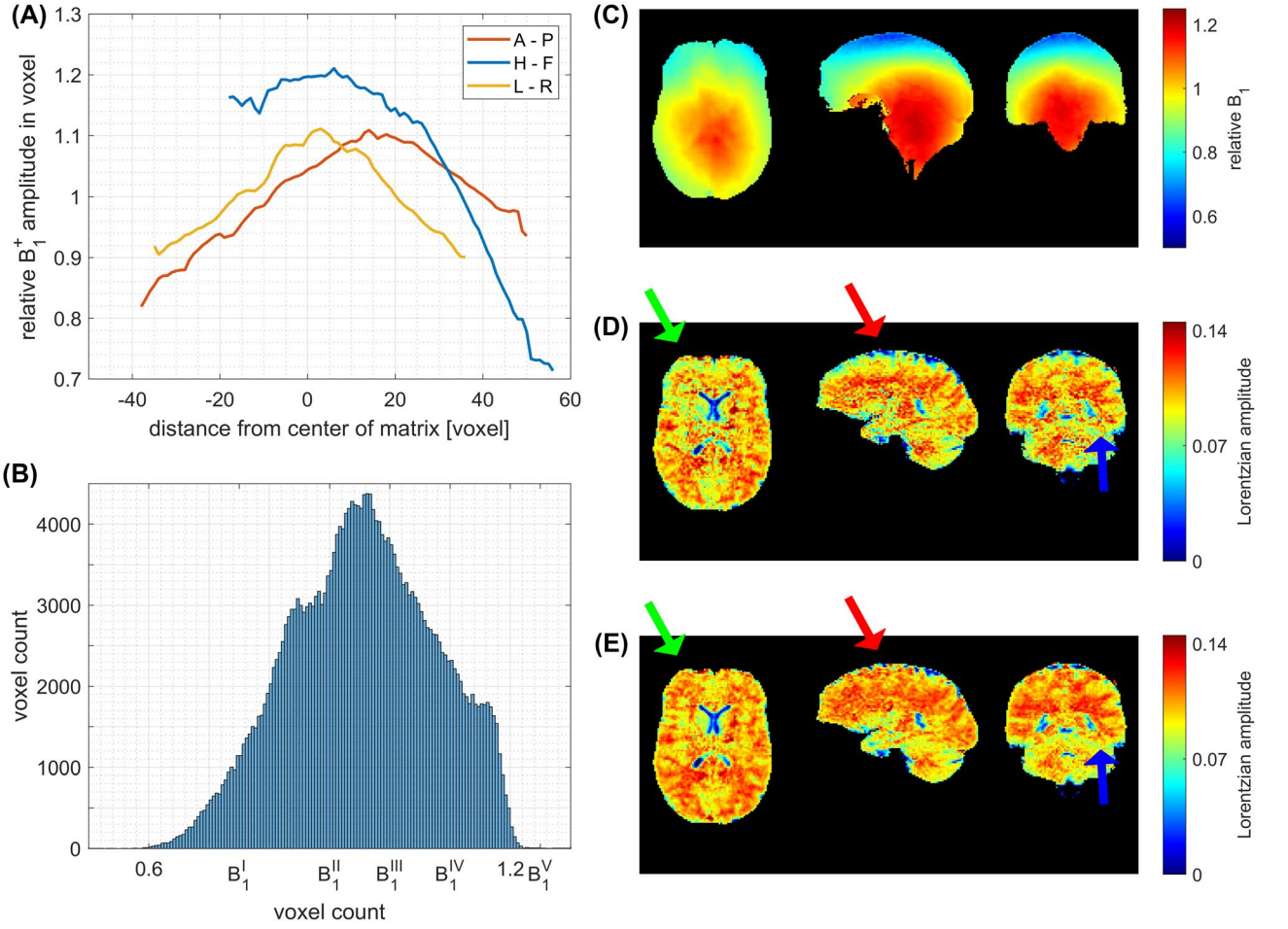

FIGURE 3 (A) Spatial distribution of relative B_1 along different directions at $B_0 = 3$T. (B) Labels B_1^I, …, B_1^V indicate the different nominal B_1 values that were measured for B_1 correction in this case. (C) B_1 distribution in slices of different orientation. Fitted rNOE CEST amplitudes without (D) B_1 correction and with Z-B_1 correction including three B_1 values (E). rNOE, relayed nuclear Overhauser enhancement

session (intrasubject) as well as across different subjects (intersubject). The intrasubject coefficients of variation (COV) in fitted amplitudes were below 8.5% for examinations in the same session and below 7% for examinations in different sessions for APT, ssMT, and rNOE both in GM and WM (Figure 7A,B). It was found that ssMT showed four times higher COV than the other fitted amplitudes when evaluated for examinations within same session. The intersubject COV was below 4% for $n = 3$ subjects (Figure 6C) for all tissues and CEST pool amplitudes. In this case, none of the fitted amplitudes showed a manifold increased COV as compared to the others within both tissue types at the same time.

3.4 | Comparison with 3D-GRE protocol

Both GRE and EPI readout were compared at an isotropic resolution of 2.34 mm with same CEST presaturation module. Still, even at a higher resolution of 1.8 mm, the EPI (black dash-dotted line, Figure 1A) outperformed the GRE at 2.34 mm isotropic resolution (red dashed line, Figure 1D) in terms of tSNR. At $(2.34\ \text{mm})^3$, the tSNR of EPI was approximately two times higher than that of the GRE (Figure 1D). CEST measurements were acquired in the same volunteer but in different sessions. EPI was applied with matrix size 110 × 96 × 72 (RO × PE × 3D: head–foot × anteroposterior × left–right) and had a total acquisition time of 4:09 minutes for 58 offsets including the unsaturated M_0 image. On the contrary, the GRE was executed with matrix size 96 × 78 × 72 (RO × PE × 3D: head–foot × anteroposterior × left–right) and took 4:59 minutes. Readout durations were 1.7 seconds for GRE and 0.8 seconds for EPI, which also showed less blurring in the raw images (Figure 7, last row).

Considering the fitted CEST amplitude maps (Figure 7), it was found that the EPI readout allowed to detect finer anatomical structures in the brain. Especially the fitted amplitudes of rNOE were more blurry using the GRE readout. Still, both readouts yielded fitted CEST amplitudes in GM and WM segments that deviated by less than 10% (Table 1). The contrast ratios between GM/WM were found to be comparable with {0.9, 1.2, 1.6} (EPI) and {0.9, 1.1, 1.4} (GRE) for APT, rNOE and ssMT.

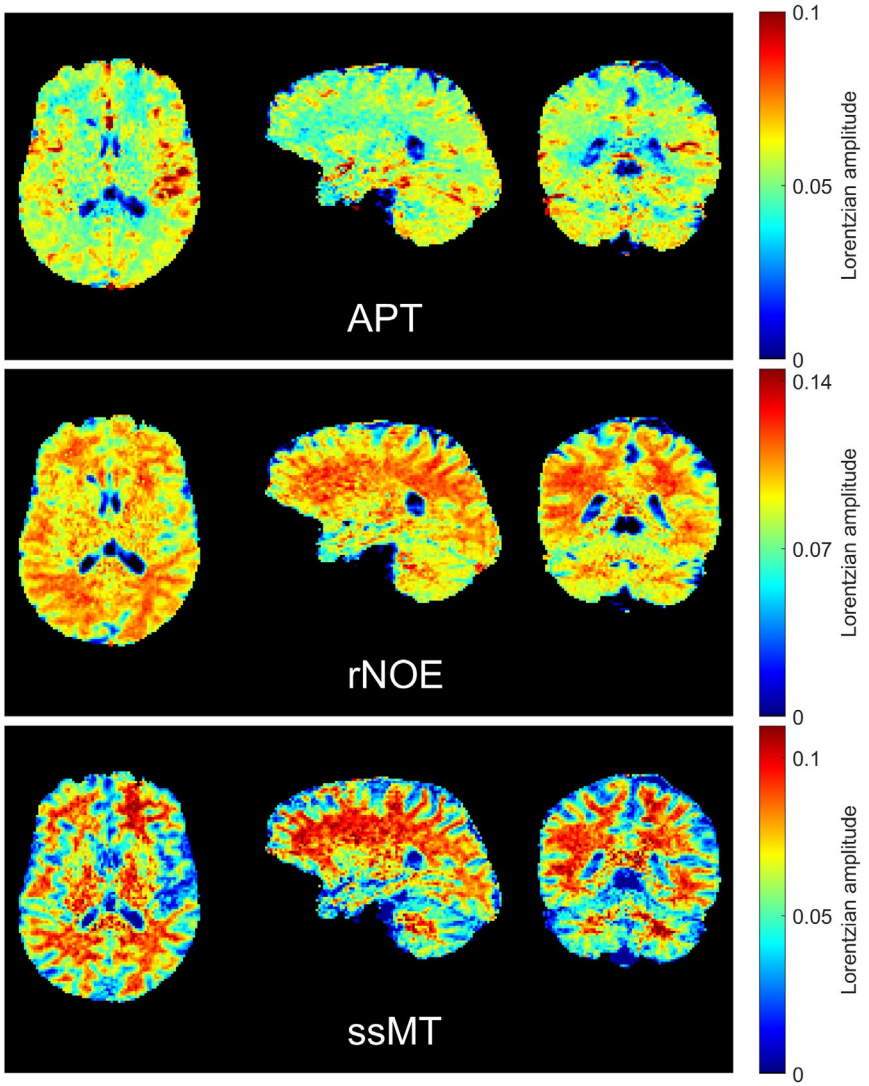

FIGURE 4 CEST contrast (Lorentzian amplitude) of 1.8 mm isotropic EPI readout. Postprocessing included motion, B_0 and B_1 correction, and PCA denoising prior to B_1 correction. Maps show amplitudes derived from 4-pool Lorentzian fits: upper row is APT; middle is rNOE; and lower row is ssMT. Contrasts are homogenous within a certain tissue type across the whole volume. Spatial resolution is high enough to, for example, recognize structures like caudate nucleus within the basal ganglia and at the same time distinguish GM and WM sections in the cerebellum. APT, amide proton transfer; GM, gray matter; PCA, principal component analysis; rNOE, relayed nuclear Overhauser enhancement; ssMT, semisolid magnetization transfer; WM, white matter

TABLE 1 Comparison of derived CEST contrast to other study

	APT		rNOE		ssMT	
	GM	WM	GM	WM	GM	WM
Deshmane et al[6]	(2.92 ± 0.24)	(2.44 ± 0.24)	(6.08 ± 0.47)	(6.44 ± 0.44)	(7.52 ± 0.04)	(10.96 ± 0.43)
GM/WM ratio	1.20		0.94		0.69	
This study EPI RO	(5.9 ± 0.1)	(5.21 ± 0.02)	(9.2 ± 0.3)	(10.8 ± 0.1)	(5.21 ± 0.09)	(8.4 ± 0.1)
GM/WM ratio	1.13		0.85		0.62	
Deshmane et al/this study	0.49	0.47	0.66	0.60	1.44	1.30
This study GRE RO	5.58	5.26	8.97	10.03	5.42	7.64
GM/WM ratio	1.06		0.89		0.71	

APT, amide proton transfer; GM, gray matter; GRE, gradient echo; rNOE, relayed nuclear Overhauser enhancement; RO, readout; ssMT, semisolid magnetization transfer WN, white matter.

3.5 | Influence of denoising

To estimate systematic effects of PCA denoising on the appearance of the Z-spectrum, the average spectrum in a homogeneous WM region of interest was considered. Supporting information Figure S6 shows that the residual Z-values due to PCA denoising according to Median criterion[17,18] are noise-like across different presaturation offsets. The maximum difference with and without denoising was 0.4% at 0.1 ppm. The average value of residual Z-value across all offsets was

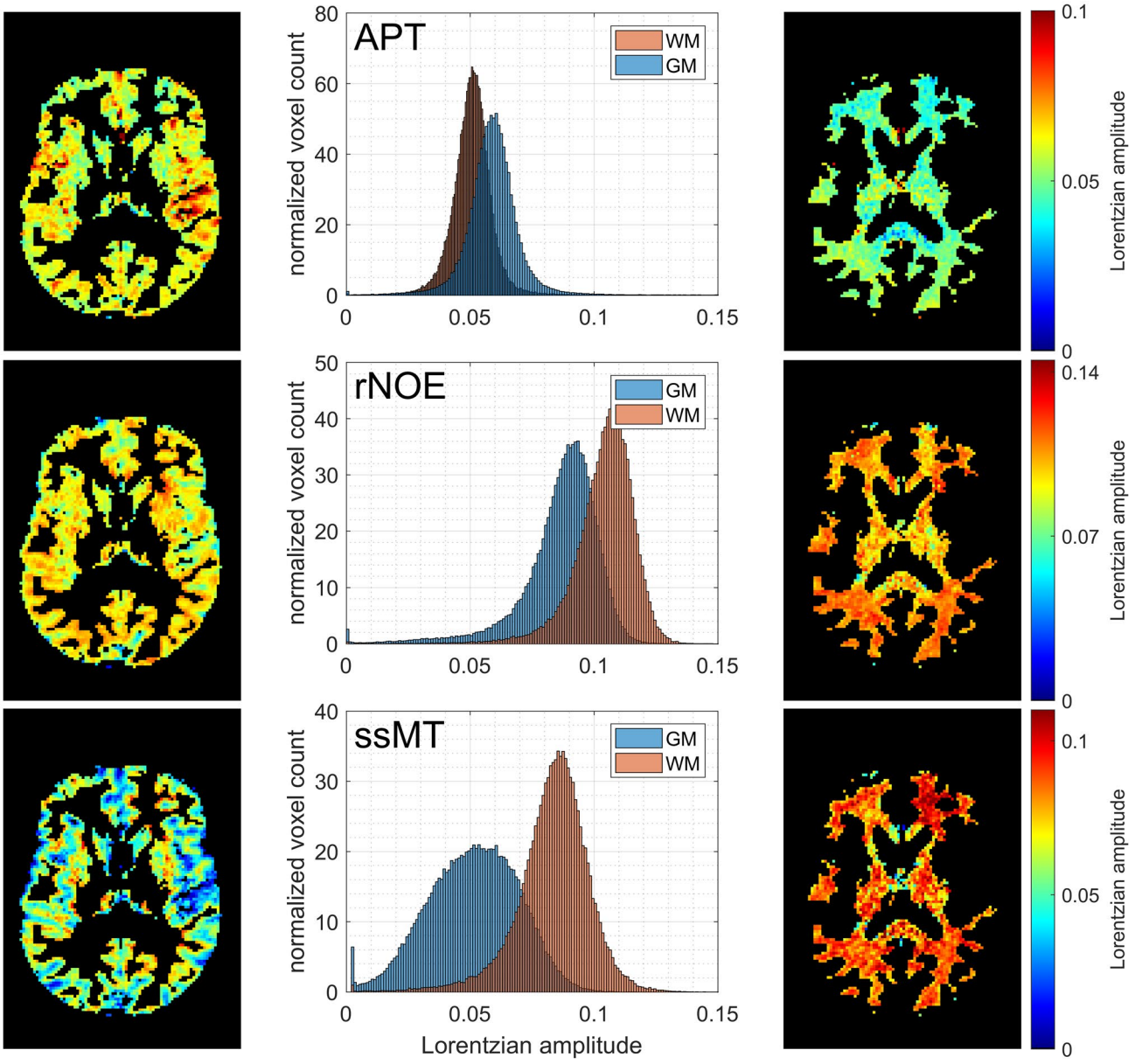

FIGURE 5 Exemplary distribution of fitted CEST contrasts (Lorentzian amplitude) in GM and WM regions: APT, rNOE, and ssMT. GM and WM regions show significant differences in distribution of all three CEST contrasts ($P < .005$). APT, amide proton transfer; GM, gray matter; rNOE, relayed nuclear Overhauser enhancement; ssMT, semisolid magnetization transfer; WM, white matter

-5.6×10^{-6}, and the average spatial SD in the non-denoised Z-spectrum was 1.0×10^{-3}. The resulting fitted amplitudes did not reveal anatomical structures depending on the denoising, as shown in Supporting Information Figure S7 and S8. In addition to the suggested postprocessing that includes PCA denoising using the Median criterion, stronger denoising with application of Malinowski's indicator function[20] was investigated. This had previously been applied in the studies of Goerke et al[24] and Deshmane et al.[6] In our study, Malinowski's indicator function suggested to include roughly 40% of the number of components suggested by the Median criterion. It was observed that this made, for example, the structures in the striatum-especially the putamen-more clearly visible in the fitted amplitude maps (Figure 8). The differences in fitted amplitudes between the two cutoff criteria did not show obvious anatomical structure besides some areas in the CSF (Supporting Information Figure S9B,C,D). The coefficients of variation of the medians of fitted amplitudes in GM and WM for both cutoff criteria were less than 1.4% for APT, rNOE, and ssMT (Supporting Information Figure S9A).

4 | DISCUSSION

It was shown that with the worked-out 3D-EPI readout, a tSNR of 75 could be achieved in all regions of the brain,

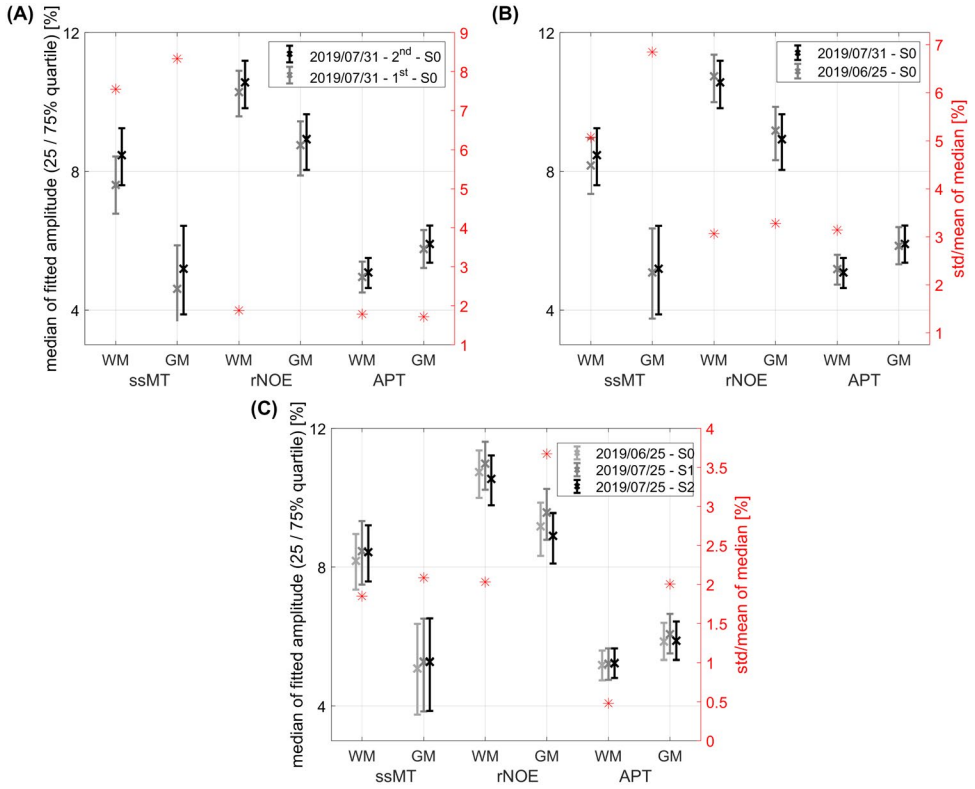

FIGURE 6 Comparison of fitted CEST contrasts in GM and WM of healthy subjects. Within same session and volunteer (A) and in different sessions (B). Across n = 3 sessions and volunteers (C); variations in fitted CEST contrasts calculated as (SD/mean over tissue type) are comparable within the same volunteer and across volunteers. Fitted CEST contrasts are stable with coefficient of variation (SD/mean) less than 9%. APT, amide proton transfer; GM, gray matter; rNOE, relayed nuclear Overhauser enhancement; ssMT, semisolid magnetization transfer; WM, white matter

even at 1.8 mm isotropic resolution at sixfold acceleration. Compared to higher field strengths (for example: Ref. 4), the approach at $B_0 = 3T$ benefits from more homogeneous saturation and excitation, especially in lower regions of the brain. In addition, the 3D-EPI readout benefits from lower field strength such that T_2 is increased by about 65% compared to 7T.[11] Assuming T_2^* scales similar as T_2 with field strength, at the given echo train length of ≈ 25 ms this is 30% higher residual transversal magnetization at the end of the readout (assuming monoexponential decay and linear scaling of magnetization with field strength), compensating partly for lower SNR as compared to ultrahigh field. The final protocol based on 3D-EPI allowed to perform CEST MRI at 1.8 mm isotropic resolution within 4.3 s per presaturation offset (1.2 s readout duration) with 256 × 224 × 156 mm^3 whole brain coverage. A previous approach of Zhu et al[25] at 3T enabled a FOV = 212 × 212 × 132 mm^3 at (2.2 $mm)^2$ in-plane resolution in 20 s per presaturation offset. A more recent 2D-EPI–based study of Ellingson et al[26] reported (2 $mm)^2$ in-plane resolution with FOV = 256 × 256 × 100 mm^3 in approximately 14 s per presaturation offset, also at $B_0 = 3T$. Krishnamoorthy et al[27] had chosen a FLASH approach with two shots per readout volume at $B_0 = 7T$. This enabled high in-plane resolution of (0.6 $mm)^2$ with a FOV of 140 × 140 × 48 mm^3 for 16 slices but took 16 s per saturation offset and did not provide whole brain coverage. Deshmane et al[6] worked with a 3D-GRE based snapshot approach, yielding (1.7 $mm)^2$ in-plane resolution for 18 slices with FOV = 220 × 180 × 54 mm^3 and 2.9 s readout. In general, snapshot-based approaches benefit from additional freedom in the presaturation such that no specific magnetization preparation has to be achieved for the image readout. It can be seen that our suggested protocol offers one of the highest spatial resolutions combined with a large FOV, it is significantly faster than most of the reported approaches and is flexible due to its snapshot realization.

One remaining drawback that all whole brain approaches share is the increased B_1 inhomogeneity within the large FOV even at clinical field strength. It has been shown previously[3,28] that an effective B_1 correction strategy is a necessary prerequisite for reliable CEST quantification at ultra-high field. However, if homogeneity over the whole brain volume is aimed at, then B_1 correction becomes necessary even at 3T, as shown in this study. This prolongs the scan time significantly because it demands repeated CEST acquisitions with different B_1 scaling. Similar to the ultra-high field study,[4] in the present study measurements at [0.75, 1.00, 1.25] times the nominal B_1 were shown to

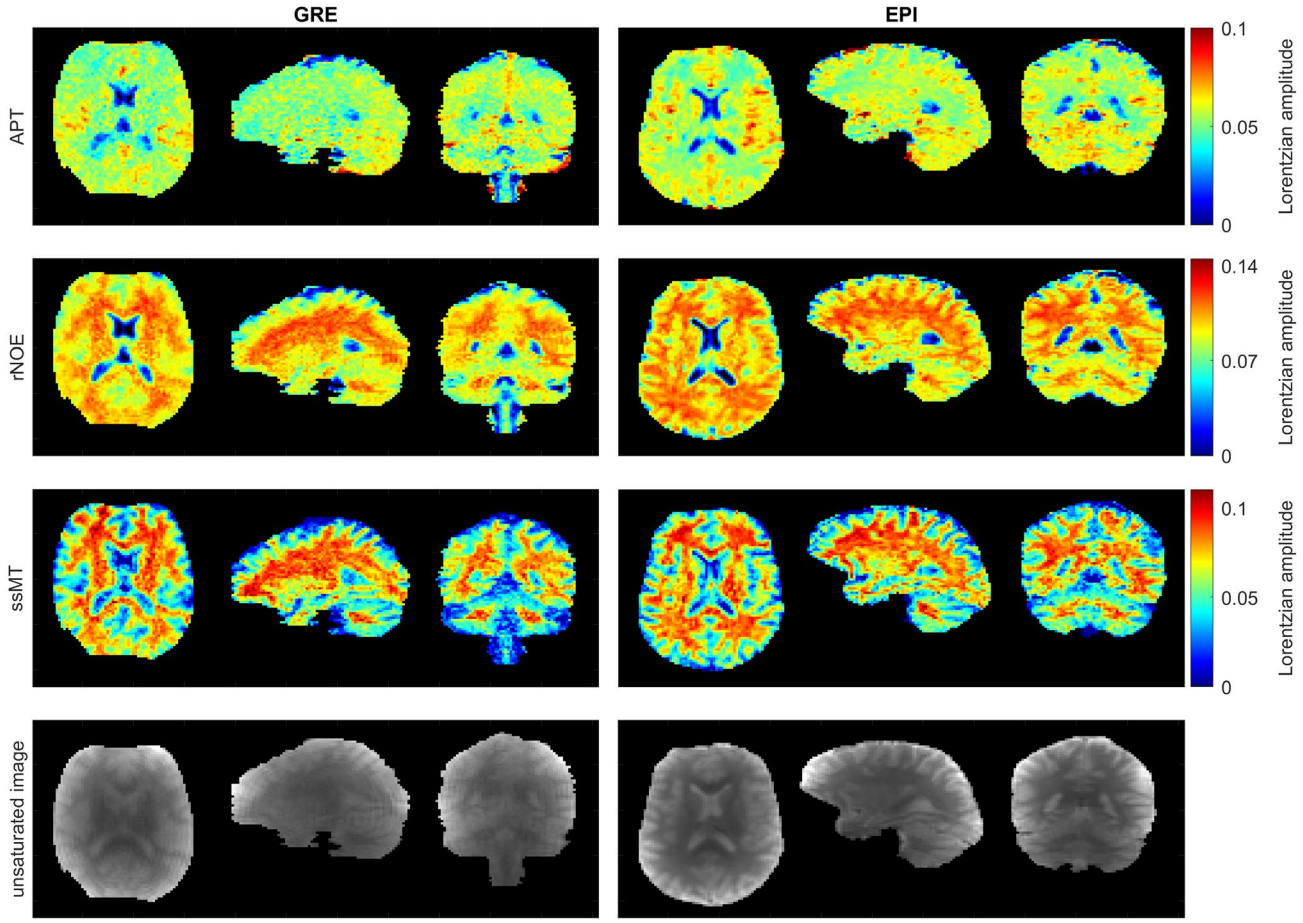

FIGURE 7 Fitted amplitudes of CEST pools: APT, rNOE, and ssMT. 2.34 mm isotropic resolution GRE (left) and EPI (right) both with same CEST presaturation module, same postprocessing, and in the same volunteer. Different segments were chosen for GRE and EPI readout, respectively, because data were not coregistered onto each other. Both readouts reveal similar GM and WM contrast in the fitted amplitudes of APT, rNOE, and ssMT. With the EPI readout, more detailed anatomical structures are visible. Additionally, in the last row unsaturated images are shown for both readouts. APT, amide proton transfer; GM, gray matter; GRE, gradient echo; rNOE, relayed nuclear Overhauser enhancement; ssMT, semisolid magnetization transfer; WM, white matter

be sufficient for spline interpolated Z-B_1 correction. The range of nominal B_1 values covered 95% of all occurring B_1 values and avoided extrapolation of the Z-spectra when correcting for B_1 inhomogeneity. The FWHM of the distributions of Z-values for all offsets were investigated in GM and WM separately after Z-B_1 correction. Including the three different B_1 values mentioned above and performing spline interpolation gave smaller FWHM than linear interpolation from five different B_1 values. On the contrary, including up to five B_1 values for spline interpolation only marginally decreased the FWHM further, indicating that the width of the natural distribution within the region of interest was already reached. Correction using two B_1 values yielded 44% smaller FWHM of Z-values than without correction. Still, in this case the fitted Lorentzian amplitudes were visibly altered. If parallel transmit systems are available, B_1 inhomogeneity might be further mitigated using B_1 shimming[29] or the MIMOSA approach,[30] which could directly be combined with our protocol.

If only certain brain areas are of interest, the number of scans at different presaturation B_1 values may be reduced given by the B_1 inhomogeneity in the considered slices. For example, for a single, more cranially located axial slice in which also B_0 distortions due to the air cavity of the mouth are less dominant, the B_1 deviation was below 20% (Figure 3A, Supporting Information Figure S10).

We also suggest to perform interleaved B_0 measurements after each CEST scan. This might not be of major importance as long as peaks can be fitted to the Z-spectrum. But in case that high power presaturation modules are used or asymmetry analysis is performed for evaluation,[31] alteration of B_0 inhomogeneity over time should be taken into account.[14] Necessity of repeated acquisitions at different presaturation B_1 also increased examination time, and therefore, the sensitivity to temporal variations in B_0 inhomogeneity. With accelerated field mapping methods, for example, DREAM/3DREAM[32,33] for B_1 and dual-echo EPI for B_0 mapping instead of WASABI, the duration of field mapping

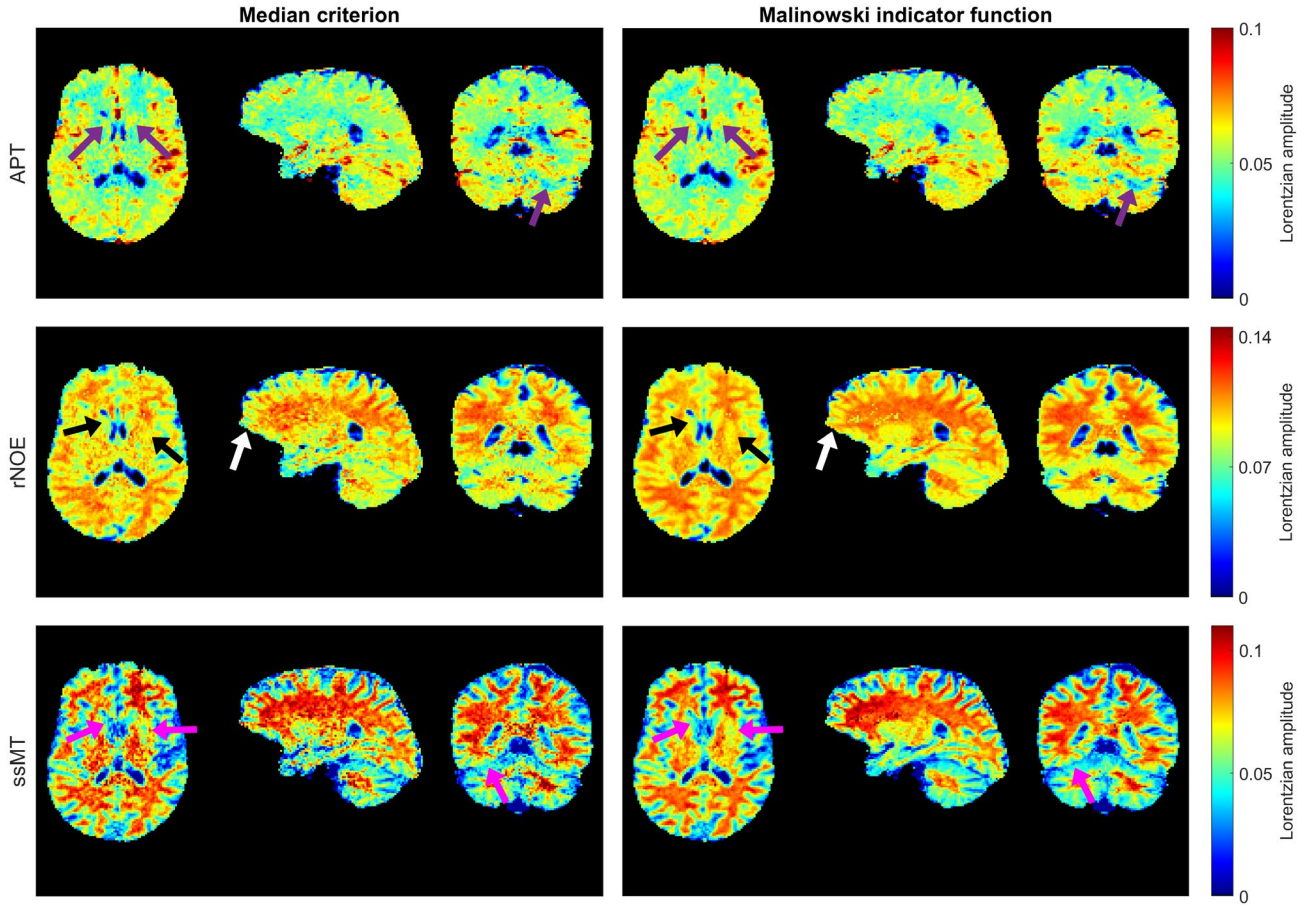

FIGURE 8 Effect of denoising on the subsequently fitted CEST pool amplitudes. APT, rNOE, and ssMT amplitudes fitted after postprocessing that included denoising according to Median (left) and Malinowski (right) criterion. Arrows highlight areas were denoising causes substantial differences in the spatial distribution of fitted amplitudes. Especially in the striatum, structures that might be of similar shape as caudate nucleus or putamen become visible when denoising with the more aggressive Malinowski criterion. APT, amide proton transfer; rNOE, relayed nuclear Overhauser enhancement; ssMT, semisolid magnetization transfer

could be strongly reduced. Assuming this enables field mapping within one minute, the total duration for the suggested procedure would be reduced by 25%. Although shorter scan durations may result in less intervolume head motion over time, retrospective motion correction before CEST analysis is still required (see Supporting Information Figure S12). Strong imaging acceleration is also an effective means to reduce intravolume motion sensitivity. Here, whole-brain k-space acquisition in only 1.2 s over 45 excitations resulted in no apparent motion artifacts. However, this may have to be reevaluated for motion-prone subject groups.

To quantify CEST effects, the amplitudes of the fitted 4-pool Lorentzian model[21] were considered. Comparable fit models had recently been applied by, for example, Deshmane et al,[6] Goerke et al,[24] and Akbey et al.[4] Medians of fitted amplitudes in GM and WM were determined separately for each subject (Supporting Information Table S2). In Table 1, the mean values over different subjects are listed. In Figures 4, 5, and 8, as well as Supporting Information Figure S13, it can be observed that especially the APT maps show some areas of strongly increased amplitudes in all healthy subjects. These match the expected spatial distribution of vessels known to have different CEST properties compared to brain tissue,[34,35] which might explain the observations in APT maps. More data on this issue can be found in Supporting Information Figure S13 to S15. Comparing the fitted CEST amplitudes to the results of Deshmane et al[6] ($B_0 = 3T$, 3D-GRE readout) showed similar behavior in GM relative to WM for APT, rNOE, and ssMT (Table 1). Nonetheless, absolute values of fitted amplitudes differed. For APT and rNOE, we derived about twice as high amplitudes as reported by Deshmane et al.[6] For ssMT, we found 1.4 times smaller amplitudes. This can be explained by the use of inversion pulses in the other study, which are known to generate strong MT effects,[36] whereas we used longer pulses for the sake of spectral selectivity. Additionally, a different number of pools was fitted to the data in both studies. Recently, Akbey et al[4] presented a CEST study at ultra-high field ($B_0 = 7T$, 3D-EPI readout). The reported GM/WM ratios (MTR_{LD} metric[23];

data extracted from Figure 9 in Ref. 4) of APT, rNOE, and ssMT {1.1, 0.9, 0.8} were similar to what we observed at $B_0 = 3T$. Nevertheless, it becomes obvious at this point that for all different presaturation and Lorentzian models used, standardization is missing. Most importantly, the compared EPI and GRE readouts yielded the same contrast for the same CEST presaturation and postprocessing used (Supporting Information Figure S14).

To investigate reproducibility of the suggested CEST pipeline, the median of the fitted amplitudes was considered. The COV across three subjects and sessions was below 4% for APT, rNOE, and ssMT. Still, it was up to 8.3% for ssMT in GM when comparing the results of repeated examinations of the same subject in the same session. On the contrary, for APT and rNOE amplitudes, it was below 2% for these two data sets. The increased deviation in the ssMT amplitudes may have several contributions. One explanation could be different GM and WM segmentation that was performed independently for different examinations. Segmentation tissue volume of both data sets differed by 0.45% for WM and 0.87% for GM. Because ssMT amplitudes show larger GM/WM contrast than those of APT and rNOE, a different segmentation should affect ssMT stronger. Still, segmentation could not exclusively be concluded to explain the observed deviations in the ssMT amplitudes. The deviations rather indicate that with the suggested CEST pipeline fitted amplitudes can at worst be reproduced with a COV of less than 8.5%.

The determined Lorentzian peaks might be used to calculate more sophisticated CEST contrasts such as the apparent exchange–dependent relaxation,[37] which additionally considers differences in T_1 relaxation times. One exemplary apparent exchange–dependent relaxation evaluation is shown in the Supporting Information Figure S11, with T_1 estimated using the proposed 3D-EPI readout in a saturation recovery protocol.

We also directly compared the proposed 3D-EPI protocol to an established 3D-GRE–based whole brain protocol.[12] EPI outperformed the GRE readout in terms of tSNR by a factor of two at the highest possible nominal resolution of the GRE, which was 2.34 mm isotropic. In addition, for the described settings the EPI readout was more than two times faster than the GRE. This gain in tSNR, along with the reduction in measurement time, allowed increased spatiotemporal resolution in the CEST acquisition as presented in this work. Fitted CEST amplitudes revealed much more detailed anatomical structures of the brain in case of the EPI readout, as shown in Figure 7. Still, GM/WM ratios of fitted amplitudes derived with the established GRE readout {1.06, 0.89, 0.71} were comparable to that observed with EPI (Table 1). It seems that actually the 3D-GRE was at its limits in case of the presented whole brain settings, for example, leading to more blurry images compared to the 3D-EPI and an established slab-selective 3D-GRE. The latter revealed contrast maps very similar to the nonselective 3D-EPI (Supporting Information Figure S14).

CEST spectra can be strongly affected by direct saturation of fat signals.[38,39] Thus, a water excitation enables mitigation of this artifact. However, binominal water excitation pulses[9] are rather long (additional ≈ 1.1 ms per excitation for both GRE and EPI) and would prolong a GRE readout significantly. Fortunately, for the EPI much fewer excitations are needed compared to GRE (45 at 1.8 mm isotropic resolution vs. 487 for the GRE at 2.34 mm), and these longer pulses can easily be afforded regarding scan time for EPI. Thus, artifacts in the Z-spectrum originating from fat signals are directly suppressed in snapshot EPI. In general, the faster readout of EPI is beneficial when comparing the PSF of GRE and EPI. Overall T_1 signal decay during readout can be described by a Look–Locker decay[2,40,41] in both cases. Assuming a T_1 of 950 ms,[11] this yields a decay to 6.4% of the initial signal amplitude for EPI after acquisition of one 3D volume and 0.55% for GRE (EPI at 1.8 mm and GRE at 2.34 mm isotropic resolution). For EPI along the first PE direction (anteroposterior), signal decay is governed by T_2^*. Still, with $T_2^* = 30$ ms, approximately 40% of the initial signal remains at the end of the considered PE-line (one PE-line containing up to 32 readout lines was encoded per excitation).

To improve SNR, PCA denoising[17] was applied during the postprocessing for both GRE and EPI, with cutoff eigenvalue determined according to Median criterion. A more aggressive denoising as introduced by Malinowski[20] was found to provide better visibility of anatomical structures in the striatum. We found that the COV due to different denoising was below 1.4% for the fitted Lorentzian amplitudes. Difference maps of amplitudes revealed no anatomical structures, but contiguous areas with larger deviations that are not noise-like (Supporting Information Figure S9) were observed. Also, Breitling et al[17] reported that Malinowski indicator function can be problematic if applied to determine the cutoff eigenvalue for CEST data. In accordance with their findings, we therefore suggest to apply the more conservative Median criterion. The chosen denoising yielded noise-like residuals when considering a region of interest in WM with and without denosing and did not alter the fitted amplitudes (Supporting Information Figure S6 to S8), which provides strong evidence for the assumption that the denoising did indeed only remove noise but did neither remove nor add systematic features to the Z-spectra.

5 | CONCLUSION

It was demonstrated that it is possible to acquire reproducible (coefficient of variation of less than 9%) CEST contrasts with whole brain coverage at $B_0 = 3T$ in 4:22 minutes per

presaturation B_1. In addition, with 1.8 mm isotropic resolution we were able to decrease the voxel size by 60% compared to currently used multislice or 3D CEST protocols. The suggested protocol is adaptable and may be used for any CEST presaturation module and fit model of interest. It therefore increases the opportunities of CEST investigations at B_0 = 3T widely.

ACKNOWLEDGMENT

The financial support of the Max Planck Society, German Research Foundation (DFG) (grant ZA 814/2-1), and European Union's Horizon 2020 research and innovation program (grant agreement No. 667510) is gratefully acknowledged.

ORCID

Sebastian Mueller https://orcid.org/0000-0003-2699-9214
Rüdiger Stirnberg https://orcid.org/0000-0001-7021-1063
Klaus Scheffler https://orcid.org/0000-0001-6316-8773
Tony Stöcker https://orcid.org/0000-0002-8946-9141
Moritz Zaiss https://orcid.org/0000-0001-9780-3616

REFERENCES

1. Grad J, Bryant RG. Nuclear magnetic cross-relaxation spectroscopy. *J Magn Reson (1969)*. 1990;90:1-8.
2. Zaiss M, Ehses P, Scheffler K. Snapshot-CEST: Optimizing spiral-centric-reordered gradient echo acquisition for fast and robust 3D CEST. *NMR Biomed*. 2018;31:e3879.
3. Windschuh J, Zaiss M, Meissner J-E, et al. Correction of B1-inhomogeneities for relaxation-compensated CEST imaging at 7 T. *NMR Biomed*. 2015;28:529-537.
4. Akbey S, Ehses P, Stirnberg R, Zaiss M, Stöcker T. Whole-brain snapshot CEST imaging at 7 T using 3D-EPI. *Magn Reson Med*. 2019;82:1741-1752.
5. Breuer FA, Blaimer M, Heidemann RM, Mueller MF, Griswold MA, Jakob PM. Controlled aliasing in parallel imaging results in higher acceleration (CAIPIRINHA) for multi-slice imaging. *Magn Reson Med*. 2005;53:684-691.
6. Deshmane A, Zaiss M, Lindig T, et al. 3D gradient echo snapshot CEST MRI with low power saturation for human studies at 3T. *Magn Reson Med*. 2019;81:2412-2423.
7. Stirnberg R, Huijbers W, Brenner D, Poser BA, Breteler M, Stöcker T. Rapid whole-brain resting-state fMRI at 3 T: Efficiency-optimized three-dimensional EPI versus repetition time-matched simultaneous-multi-slice EPI. *Neuroimage*. 2017;163:81-92.
8. Poser BA, Ivanov D, Kannengiesser SA, Uludag K, Barth M. Accelerated 3D EPI using 2D blipped-CAIPI for high temporal and/or spatial resolution. In Proceedings of the 22nd Annual Meeting of ISMRM, Milan, Italy, 2014. p. 1506.
9. Stirnberg R, Brenner D, Stöcker T, Shah NJ. Rapid fat suppression for three-dimensional echo planar imaging with minimized specific absorption rate. *Magn Reson Med*. 2016;76:1517-1523.
10. Griswold MA, Jakob PM, Heidemann RM, et al. Generalized autocalibrating partially parallel acquisitions (GRAPPA). *Magn Reson Med*. 2002;47:1202-1210.
11. Zhu J, Klarhöfer M, Santini F, Scheffler K, Bieri O. Relaxation measurements in brain tissue at field strengths between 0.35T and 9.4T. In Proceedings of the 22nd Annual Meeting of ISMRM, Milan, Italy, 2014. Abstract 3208.
12. Mueller S, Deshmane A, Herz K, Scheffler K, Zaiss M. Development of whole-brain 3D snapshot CEST MRI at 3T. In Proceedings of the 27th Annual Meeting of ISMRM, Montréal, Québec, Canada, 2019. Abstract 3995.
13. Schuenke P, Windschuh J, Roeloffs V, Ladd ME, Bachert P, Zaiss M. Simultaneous mapping of water shift and B1 (WASABI)—Application to field—Inhomogeneity correction of CEST MRI data. *Magn Reson Med*. 2017;77:571-580.
14. Windschuh J, Zaiss M, Ehses P, Lee J-S, Jerschow A, Regatte RR. Assessment of frequency drift on CEST MRI and dynamic correction: Application to gagCEST at 7 T. *Magn Reson Med*. 2019;81:573-582.
15. Cox RW. AFNI: Software for analysis and visualization of functional magnetic resonance neuroimages. *Comput Biomed Res*. 1996;29:162-173.
16. Ashburner J, Friston KJ. Unified segmentation. *NeuroImage*. 2005;26:839-851.
17. Breitling J, Deshmane A, Goerke S, et al. Adaptive denoising for chemical exchange saturation transfer MR imaging. *NMR Biomed*. 2019;e4133.
18. Manjón JV, Coupé P, Buades A. MRI noise estimation and denoising using non-local PCA. *Med Image Anal*. 2015;22:35-47.
19. Malinowski ER. Theory of error in factor analysis. *Anal Chem*. 1977;49:606-612.
20. Malinowski ER. Determination of the number of factors and the experimental error in a data matrix. *Anal Chem*. 1977;49:612-617.
21. Zaiß M, Schmitt B, Bachert P. Quantitative separation of CEST effect from magnetization transfer and spillover effects by Lorentzian-line-fit analysis of z-spectra. *J Magn Reson*. 2011;211:149-155.
22. van der Zwaag W, Marques JP, Kober T, Glover G, Gruetter R, Krueger G. Temporal SNR characteristics in segmented 3D-EPI at 7T. *Magn Reson Med*. 2012;67:344-352.
23. Jones CK, Huang A, Xu J, et al. Nuclear overhauser enhancement (NOE) imaging in the human brain at 7 T. *NeuroImage*. 2013;77:114-124.
24. Goerke S, Soehngen Y, Deshmane A, et al. Relaxation-compensated APT and rNOE CEST-MRI of human brain tumors at 3 T. *Magn Reson Med*. 2019;82:622-632.
25. Zhu H, Jones CK, van Zijl PCM, Barker PB, Zhou J. Fast 3D chemical exchange saturation transfer (CEST) imaging of the human brain. *Magn Reson Med*. 2010;64:638-644.
26. Ellingson BM, Yao J, Raymond C, et al. pH-weighted molecular MRI in human traumatic brain injury (TBI) using amine proton chemical exchange saturation transfer echoplanar imaging (CEST EPI). *NeuroImage Clin*. 2019;22:101736.
27. Krishnamoorthy G, Nanga RPR, Bagga P, Hariharan H, Reddy R. High quality three-dimensional gagCEST imaging of in vivo human knee cartilage at 7 Tesla. *Magn Reson Med*. 2017;77:1866-1873.
28. Singh A, Cai K, Haris M, Hariharan H, Reddy R. On B1 inhomogeneity correction of in vivo human brain glutamate chemical exchange saturation transfer contrast at 7T. *Magn Reson Med*. 2013;69:818-824.
29. Tse DHY, da Silva NA, Poser BA, Shah NJ. B1+ Inhomogeneity mitigation in CEST using parallel transmission. *Magn Reson Med*. 2017;78:2216-2225.

30. Liebert A, Zaiss M, Gumbrecht R, et al. Multiple interleaved mode saturation (MIMOSA) for B1+ inhomogeneity mitigation in chemical exchange saturation transfer. *Magn Reson Med*. 2019;82:693-705.
31. Guivel-Scharen V, Sinnwell T, Wolff SD, Balaban RS. Detection of proton chemical exchange between metabolites and water in biological tissues. *J Magn Reson*. 1998;133:36-45.
32. Ehses P, Brenner D, Stirnberg R, Pracht ED, Stöcker T. Whole-brain B1-mapping using three-dimensional DREAM. *Magn Reson Med*. 2019;82:924-934.
33. Nehrke K, Börnert P. DREAM – A novel approach for robust, ultrafast, multislice B1 mapping. *Magn Reson Med*. 2012;68:1517-1526.
34. Shah SM, Mougin OE, Carradus AJ, et al. The z-spectrum from human blood at 7T. *Neuroimage*. 2018;167:31-40.
35. Zheng S, van der Bom IMJ, Zu Z, Lin G, Zhao Y, Gounis MJ. Chemical exchange saturation transfer effect in blood. *Magn Reson Med*. 2014;71:1082-1092.
36. McLaughlin AC, Ye FQ, Pekar JJ, Santha AKS, Frank JA. Effect of magnetization transfer on the measurement of cerebral blood flow using steady-state arterial spin tagging approaches: A theoretical investigation. *Magn Reson Med*. 1997;37:501-510.
37. Zaiss M, Xu J, Goerke S, et al. Inverse Z-spectrum analysis for spillover-, MT-, and T1 -corrected steady-state pulsed CEST-MRI–application to pH-weighted MRI of acute stroke. *NMR Biomed*. 2014;27:240-252.
38. Zimmermann F, Korzowski A, Breitling J, et al. A novel normalization for amide proton transfer CEST MRI to correct for fat signal–induced artifacts: Application to human breast cancer imaging. *Magn Reson Med*. 2020;83:920-934.
39. Lu J, Zhou J, Cai C, Cai S, Chen Z. Observation of true and pseudo NOE signals using CEST-MRI and CEST-MRS sequences with and without lipid suppression. *Magn Reson Med*. 2015;73:1615-1622.
40. Look DC, Locker DR. Time saving in measurement of NMR and EPR relaxation times. *Rev Sci Instrum*. 1970;41:250-251.
41. Ganter C. Analytical solution to the transient phase of steady-state free precession sequences. *Magn Reson Med*. 2009;62:149-164.

SUPPORTING INFORMATION

Additional Supporting Information may be found online in the Supporting Information section.

FIGURE S1 tSNR evaluation at $B_0 = 3T$ for 63 images with 3 s idle time between subsequent acquisitions. Final protocol as described in the paper was applied with different nominal flip angles ranging from 10 to 30 degree. All data were corrected for motion during post processing. Besides the flip angle all parameters remained unchanged: (1.78 mm)³ nominal resolution, CAIPIRINHA = $1 \times 6^{shift=2}$, half elliptical scanning, BW = 1930 Hz/pix, phase partial Fourier and FOV = 256 × 224 × 156 mm³

FIGURE S2 tSNR determined for 63 images with 3 s idle time between subsequent acquisitions. Final protocol was used besides the deviations stated in the legend with the dark blue line being the final settings. Data were corrected for motion

FIGURE S3 Comparison of tSNR across 63 images with 3 s idle time in between subsequent acquisitions. The novel 3D-EPI protocol worked out for 3 T yields approximately 20% higher tSNR as the published 7T protocol.[1] Both protocols were executed at (1.78 mm)³ nominal resolution, FA = 15° and BW = 1930 Hz/pix and motion correction was performed

FIGURE S4 (A) shows the relative magnitude rMag for different FA with its maximum value of 4.4% for a FA = 17.5°. (B) shows the relative FWHM (rFWHM) for the 3T protocol with different flip angles (FA). It can be seen that for FA = 15° the average rFWHM is increased to ≈1.34

FIGURE S5 (A) Effect of Z-B_1 correction (3) on the distribution of Z-values in gray matter at presaturation offset −3.5 ppm. Effect of 2 (B) to 5 (E) B_1 values included in Z-B_1 correction on fitted rNOE amplitudes. Including 2 (B) values (linear interpolation) shows deviations as compared to 5 values (spline interpolation) included. Difference between 3 and 4 or 5 values included (all: spline interpolation) is only little

FIGURE S6 Influence of denoising according to the Median criterion on the mean Z-spectrum in a white matter region of interest in a healthy volunteer. The mean Z-spectrum did not significantly differ after denoising which is shown, for example, in the difference of the Z-spectra. The mean value of difference is -5.6×10^{-6}, whereas the spatial standard deviations are on average 1.0×10^{-3max} (without PCA) and 9.4×10^{-4} (including PCA), respectively

FIGURE S7 Comparison of fit results in a healthy volunteer with respect to the effect of PCA denoising (cut off eigenvalue determined according to the Median criterion). Plots show correlation of fitted Lorentzian amplitudes with and without PCA denoising. Legends provide: Pearson r, P-value as well as slope and offset of a linear fit to the data. High correlation of $r > 0.92$ for all contrasts (APT, rNOE, ssMT and (direct saturation) DS) indicates that PCA denoising does not intorduce any systematical bias to the fit results

FIGURE S8 Fitted Lorentzian amplitudes of APT, rNOE, SSMT and DS (direct saturation) are shown in the same axial slice separately with and without PCA denoising (cut off eigenvalue determined according to the Median criterion). Last row shows the difference between the two sets of fitted amplitudes. The difference maps do not reveal any significant anatomical structure that would have potentially been introduced due to the PCA denosing

FIGURE S9 Effect of different cut off criteria during PCA denoising (17) on the fitted CEST amplitudes of one healthy subject (S0). (A): median of ssMT, rNOE and APT amplitudes in gray and white matter for cut off according to Malinowski's indicator function (20) and Median criterion (18). The maps in (B), (C) and (D) show spatial distribution of the difference in fitted amplitudes of the same data shown in (A). Arrows indicate contiguous areas of deviations

FIGURE S10 Fitted amplitudes of APT (A), rNOE (B) and ssMT (C) for a different number of B_1 values included in the B_1 correction (3). Maps show axial slice in more cranially situated

region of the brain that had more homogeneous B_1 distribution than other areas of the brain. B_1 correction including only two different B_1 values (linear interpolation) might, therefore, be sufficient. Still including five B_1 values and applying spline interpolation yields smoother maps due to averaging

FIGURE S11 CEST MRI acquired according to the final protocol combined with a saturation recovery sequence to determine T_1 and from this calculate the T_1 corrected AREX (37) contrast

FIGURE S12 Same data and post processing but once with and once without motion correction. Arrows highlight areas were substantial differences in the fitted Lorentzian amplitudes can be seen if motion correction is not applied. Even though the optimized protocol allows relatively fast CEST MRI acquisition motion would significantly corrupt the results if not corrected

FIGURE S13 Fitted Lorentzian amplitudes (rNOE, APT, ssMT and (DS) direct saturation) of four healthy volunteers. For all volunteers only in the APT maps voxels with much larger amplitudes are visible

FIGURE S14 Fitted Lorentzian amplitudes and maximum intensity projections for an established slab selective 3D-GRE (2,6) and the novel non-selective 3D-EPI readout. In both cases only in the APT maps similarly shaped and located areas show higher amplitudes (see arrows). Both readouts were acquired in different volunteers, and therefore, have different slice orientations. Data includes slices 2 to 11 (GRE) and 87 to 100 (EPI), respectively

FIGURE S15 Same 3D-EPI measurement as shown in Supporting Information Figure S15. Residual sum of saqures (RSS) was determined in slice 87 to 100. It is found that RSS does not increase with increasing APT amplitudes (A) and that highest RSS is observed in the ventricles

TABLE S1 Fit parameters for all $i = 0, \ldots, 3$ amplitudes (Ai), peak widths (Gi), initial magnetization (Zi) and position of the bulk water pool (dwi). Positions for $i = 1, \ldots, 3$ were fixed at 3.1, −1.25 and −3.1 ppm relative to dwi. Other parameters fitted with lower bond (lb), upper bond (ub) and start values (p0)

TABLE S2 Resulting amplitudes of 4-pool Lorentz fit for $n = 5$ different examinations in 3 different subjects (S0, S1 and S2). All values are given in percent to increase visibility. For each examination and subject median and standard deviation (std) were determined in gray (GM) and white matter (WM) for APT, rNOE and ssMT. In the 3 bottom lines mean, standard deviation and coefficient of variation (c.o.v.) across the five different examinations are shown

How to cite this article: Mueller S, Stirnberg R, Akbey S, et al. Whole brain snapshot CEST at 3T using 3D-EPI: Aiming for speed, volume, and homogeneity. *Magn Reson Med*. 2020;84:2469–2483. https://doi.org/10.1002/mrm.28298